

# Bachelor Thesis

## Finding an Optimal Regularisation Parameter for the Inversion of Transient Electromagnetic Data Using the L-Curve Method

Peter Balogh

e12202337@student.tuwien.ac.at

Matr.Nr. 1220 2337

Date: October 16, 2025

Supervisor: Associate Prof. Dr.rer.nat. Adrian Flores-Orozco

### Abstract

## 1 Introduction

## 2 Materials and Methods

### 2.1 State of the Art

#### 2.1.1 Common resistivity values

Electrical resistivity is a key parameter in geophysical investigations, as it provides valuable information about the properties of the Earth's subsurface. Many electrical and electromagnetic methods rely on constructing a model of the electrical resistivity distribution to characterise subsurface materials. By analysing these resistivity values, it is possible to infer the composition of subsurface layers and detect geological structures such as faults, fractures, and aquifers (Christiansen et al. 2006).

Table 1 presents commonly reported resistivity values for different subsurface materials. These values have been compiled from multiple studies conducted in diverse geological settings and using various geophysical methods (Gómez et al. 2019; Galazoulas et al. 2015; George et al. 2021).

**Tab. 1:** Common Resistivity Values of Subsurface Materials

Material	Resistivity ( $\Omega\text{m}$ )
Saturated layers with high salinity	0.1 – 5
Saturated clays and silts	5 – 15
Saturated sediments	10 – 20
Unsaturated sediments	50 – 80
Saturated sand	40 – 150
Unsaturated sand	400 – 1500

In the context of Table 1, the term “sediments” refers to unconsolidated deposits consisting of a mixture of sand, silt, and clay. The precise resistivity values presented in Table 1 for sediments are not general global values but are specific to the study region investigated by Gómez et al. (2019). These values reflect the characteristics of sediments found in the Challapampa aquifer in Bolivia, where variations in grain size, moisture content, and mineral composition influence the resistivity measurements.

#### 2.1.2 Transient Electromagnetic method

The transient electromagnetic (TEM) method is a geophysical technique developed for sub-

surface exploration and mineral prospecting in the 1980s. It is a time-domain electromagnetic method that can be used to infer information about the electrical conductivity distribution of the Earth's subsurface. As an electromagnetic wave propagates through the subsurface, it is attenuated by the electrical properties of the materials it encounters. The Maxwell equations govern that a changing electrical field induces a magnetic field, and vice versa. For the TEM method a pulse of current is transmitted through a transmitter loop generating a primary magnetic field. When the current is turned off, the decay of the primary field induces secondary currents (eddy currents) in the ground, which produce a secondary electromagnetic field. This field is measured using a receiver coil, as the strength of the secondary field depends on the conductivity of the material the EM wave propagates through. By analysing the decay characteristics of the secondary field, it is possible to infer the conductivity structure of the subsurface, because the wave propagates deeper into the subsurface, later times include information about deeper layers. Such a decay curve is called a transient and multiple transients are measured for each sounding to counteract the random noise in the measurement. An EM wave attenuates faster in conductive materials, which results in a shallower investigation depth. For this reason the TEM method was developed to find conductive materials like ores, clay, and water-bearing formations in resistive media. As the interpretation of the data is computationally intensive and requires sophisticated instruments to measure the secondary field accurately, this method is rather "young" compared to other geophysical methods like electrical resistivity tomography (ERT) and magnetotellurics (MT) (Christiansen et al. 2006).

In order to get information on the subsurface resistivity, the measured signal must be converted to an apparent resistivity ( $\rho_a$ ). This can be done by using the formula for late stage behaviour of the secondary field:

$$\rho_a = \frac{1}{\pi} \left( \frac{M}{20 \cdot \frac{\partial b_z}{\partial t}} \right)^{\frac{2}{3}} \left( \frac{\mu_0}{t} \right)^{\frac{5}{3}} \quad (1)$$

where  $M$  is the magnetic moment,  $\frac{\partial b_z}{\partial t}$  is the signal measured by the receiver coil,  $\mu_0$  is the

magnetic permeability of free space and  $t$  is the time. The magnetic moment is the product of the number of turns, the area, and the current in the transmitter loop. The apparent resistivity is a measure of the resistivity of the subsurface material the EM wave has traveled through, but it is not the true resistivity of the material. For this reason inflection points can be interpreted as boundaries between different layers with different resistivities, and the slope of the curve shows whether the resistivity is increasing or decreasing in the new layer (Fitterman et al. 1986).

Another approach is to use the inversion of the data to create a model of the subsurface resistivity. This is explained in more detail in section 2.1.4. For the interpretation of TEM data – and for the inversion in particular – some assumptions must be made: EM waves only propagate vertically and the subsurface is layered. As most inversion algorithms are work with a 1D model, the subsurface is assumed to be homogeneous in the horizontal direction. Even with these limitations the TEM method is a powerful tool for the exploration of the subsurface and can be used in various applications (Christiansen et al. 2006).

### 2.1.3 Environmental applications of TEM

Although the TEM method originates from the mining industry, it can have various environmental applications, the most common being exploration and characterisation of groundwater resources is one of the most common applications of the TEM method.

In this context, Danielsen et al. (2003) used the TEM method for the exploration of buried valleys as potential aquifers in Denmark. The study introduced two new TEM systems based on the Geonics PROTEM – the high moment transient electromagnetic (HiTEM) system for a deeper investigation depth and the pulled array Transient electromagnetic (PATEM) system for a higher lateral resolution. The HiTEM system uses a combination of a  $30 \times 30$  m transmitter loop and a current of 75 m to achieve a depth of investigation (DOI) of up to 300 m. To mitigate distortion effects, an offset receiver loop is used for the later times and a central receiver loop with a reduced current of 2.5 A for the

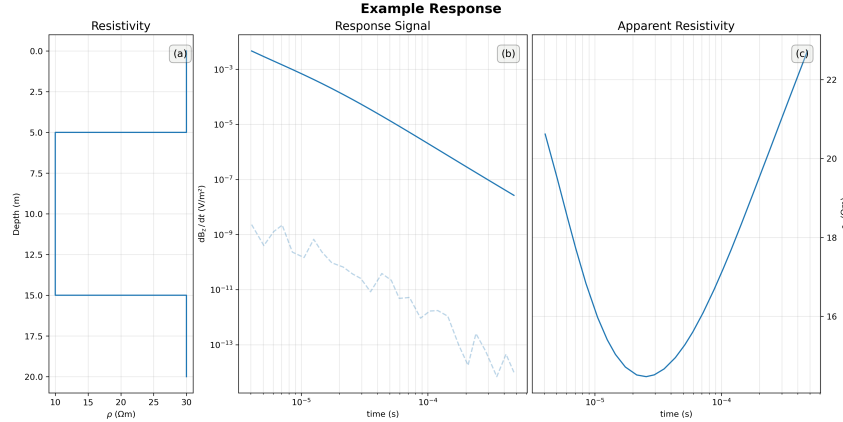


**Fig. 1:** Numerically modelled typical TEM response with the signal a) and the apparent resistivity b).

early times. A mutually constrained inversion (MCI) is used to invert the combination of the data gathered with the two different configurations. The PATEM system uses a  $3 \times 5$  m transmitter loop on a wheeled frame with an offset receiver loop. This allows for continuous measurements along a profile and a DOI of 100 – 150 m. To achieve a high DOI and useful near surface information, the PATEM system allows for a transmitter configuration with either 2 turns with 16 A or 8 turns with 40 – 50 A. The study also touches on the problems resulting from coupling with man-made structures. The coupling effects can be divided into galvanic and capacitive. Galvanic coupling is caused by grounded conductors like power lines and causes an underestimation of the resistivity. Capacitive coupling is caused by current being generated in the conductor and leaking into the ground through an insulation, which leads to an oscillating signal. For this reason the study recommends keeping a distance of about 150 m from underground cables or pipes when the earth has a resistivity of 40 – 50  $\Omega\text{m}$ . The study finds that a 1D inversion approach is sufficient to detect the slope of a 2D buried valley when in a layer with low resistivity. In a layer with high resistivity, only the overall structure of the valley can be derived.

Similarly to the PATEM system, Auken et al. (2019) propose a towed transient electromagnetic (tTEM) system for an efficient 3D mapping of the subsurface. The tTEM system utilises a  $2 \times 4$  m transmitter loop mounted on a non-conductive sled towed by a vehicle,

which enables a production rate of about 1  $\text{km}^2$  per day. The receiver loop is towed at 9 m offset from the transmitter. Like the PATEM system, the tTEM system permits the use of two different currents (2.8 and 30 A) in order to gain a relatively high DOI of up to 70 m, while still allowing the investigation of shallow depths. This study also highlights the importance of considering the coupling effects of the system with conductive objects and it tests the system in an environment with a high resistivity of the subsurface ( $> 600 \Omega\text{m}$ ). Under these circumstances the signal caused by coupling can be observed in isolation and the study found that a minimal distance of 3 m between transmitter and vehicle was necessary to mitigate coupling effects. As it is important to calibrate TEM systems, the tTEM system was validated at the Danish National TEM test site. Furthermore, the tTEM system was also validated against borehole data and the results showed a good agreement.

Electromagnetic methods do not require direct contact with the subsurface, which allowed for the development of airborne electromagnetic methods (AEM). Sørensen et al. (2004) introduced the SkyTEM system as an alternative to ground based TEM systems. The SkyTEM system uses a helicopter to carry a  $12.5 \times 12.5$  m transmitter loop with 4 turns and a receiver loop ( $0.5 \times 0.5$  m) in a central configuration. Just like the PATEM and HiTEM systems, a low moment and a high moment configuration are used to achieve a high DOI while still resolving the near surface layers. In the low moment config-

uration the current of 35 A only flows through one turn and for the high moment 50 A are used with all 4 turns. The SkyTEM system was validated against a ground based TEM system with a transmitter loop size of  $40 \times 40$  m, showing a good agreement (below 5% deviation). This system is able to cover a larger area than traditional ground based systems in the same amount of time, while still being able to resolve underground structures, such as buried valleys.

To investigate the subsurface below continental bodies of water, Aigner et al. (2021) propose a flexible single loop system which can be towed by a boat. By using a single loop which is kept afloat by several PVC pipe segments that keep it in a circular shape, the system can easily be moved around the lake. Using pipe segments allows for different loop sizes and thus different investigation depths. The TEM-FAST 48 system by Applied Electromagnetic Research (AEMR) was used to investigate the subsurface of the Lake Langau in Austria. A current of 4 A and loops with radii between  $6.2 - 11.9$  m were used, leading to an investigation depth between  $6.2 - 50.0$  m, which was sufficient to detect sedimentary layers below the lake. For a proper interpretation of early time data, it is important to understand how long the turn-off time of the transmitter for a single-loop setup is. When the transmitter is turned off, the current in the loop takes a certain amount of time to decay, which is called the turn-off ramp. This time was measured to be between  $4.2 - 10.4 \mu\text{s}$  – depending on loop size and resistivity of the subsurface. Using this information, a formula was derived to find the minimum effective sounding depth:

$$h_{\text{eff}} = \sqrt{t_{\text{eff}} \bar{\rho}} \quad (2)$$

where  $h_{\text{eff}}$  is the minimum effective sounding depth,  $t_{\text{eff}}$  is the minimum effective time and  $\bar{\rho}$  is the average resistivity of the smooth subsurface model. The study also showcased two different approaches to finding the DOI. The first uses different starting models for the inversion assuming that the DOI is reached when the data does not influence the inverted model anymore and will keep the values of the starting model. The second approach is based on:

$$\text{DOI} \approx 0.55 \left( \frac{M \times \bar{\rho}}{\eta} \right) \quad (3)$$

where  $M$  is the magnetic moment,  $\bar{\rho}$  is the average resistivity of the smooth subsurface model and  $\eta$  is the noise level. Both methods agree on a DOI ranging between 20 and 50 m depending on the loop size.

As other water sources become less reliable in some regions in Bolivia, Gonzales Amaya et al. (2018) show the potential of the TEM method for the exploration of groundwater in the Punata alluvial fan. This aquifer is an important water source, but it has zones with high salinity, which poses challenges in its use. This study used the ABEM WalkTEM system with a  $50 \times 50$  m transmitter loop with a current of 18 A and two receiver loops ( $0.5 \times 0.5$  m and  $10 \times 10$  m) in a central configuration. This way a DOI of up to 200 m was achieved in some regions of the alluvial fan, while in other regions the DOI was limited to 80 m. The study was able to detect zones with high salinity and the results were validated with borehole data.

Gómez et al. (2019) conducted a similar study in the Challapampa area, Bolivia. In this study the same WalkTEM system and loop sizes were used as in the study by Gonzales et al. Gonzales Amaya et al. 2018 However, the receiver loops were deployed in an offset configuration and for the  $0.5 \times 0.5$  m loop only a current of 2 A was used, while the whole 18 A were applied for the  $10 \times 10$  m loop. This setup achieved a depth of investigation (DOI) of up to 250 m and identified the influence of a hot spring, which appeared as a low-resistivity zone, indicating higher salinity.

Another application of TEM is the detection of karstic features, like caves, faults, and fracture zones (Zhou et al. 2022; Su et al. 2024). Traditionally, a large transmitter loop size in the order of 100 m side length was used to achieve a high investigation depth. For this reason the TEM method was not suitable for the application in mountainous regions. However, a similar investigation depth can be achieved by using a smaller transmitter loop size and more turns. A multi-turn setup has the disadvantage of mutual inductance caused by the large number of turns, which can lead to underestimation of the resistivity of the subsurface.

Zhou et al. (2022) proposed a coincident configuration with a  $2 \times 2$  m and 10 turns for the transmitter loop and 20 turns for the receiver

loop. In order to mitigate the effects of the mutual inductance, borehole and electrical resistivity tomography (ERT) data were used to constrain the inversion. Because boreholes and ERT measurements are expensive and time-consuming, they are only used to correct the TEM soundings in order to account for shifted resistivity values. This method was used to detect a karst channel in Zhijin, China.

A more in-depth study on how to deal with self and mutual inductance was conducted by Su et al. (2024). Here a central loop configuration (receiver loop in the centre of the transmitter loop) was compared with a multi-turn small fixed-loop configuration (using multiple different receiver positions, while keeping the transmitter loop fixed). For the fixed-loop set up a correction coefficient was introduced to account for off-centre receiver positions. 5 model tests were conducted in order to compare the two configurations and the results showed that after correction the fixed-loop configuration was more accurate in detecting the position of one or multiple anomalies.

#### 2.1.4 Data Inversion

A typical geophysical problem can be defined as follows:

$$\mathbf{d} = \mathcal{F}(\mathbf{m}) \quad (4)$$

where  $\mathbf{d}$  is the observed data,  $\mathcal{F}$  is the forward operator, and  $\mathbf{m}$  is the model. If the model is known, the forward operator can be used to calculate the expected data. Unfortunately, usually the model is unknown and the observed data is used to find the model, which is called an inverse problem. In practise the observed data is contaminated with noise, which introduces an error term into the equation and makes the inversion ill-posed and non-linear. An ill-posed problem means that small changes in the observed data can cause large differences in the model. As a result, noise introduces variability, making it impossible to find a unique solution (Zhdanov 2002).

Approaches to address this issue can be divided into deterministic and stochastic methods. The deterministic approach tries to find a single solution, by iteratively updating the model parameters to minimise the difference between observed and modeled data. To prevent overfit-

ting to noise, Tikhonov regularisation is used, which adds a penalty term to the least squares problem.

$$\|\mathbf{W}_d(\mathcal{F}(\mathbf{m}) - \mathbf{d})\|_2^2 + \lambda \|\mathbf{W}_m(\mathbf{m} - \mathbf{m}_0)\|_2^2 \rightarrow \min \quad (5)$$

$\mathbf{W}_d$  and  $\mathbf{W}_m$  are weighting matrices,  $\mathbf{m}_0$  is the initial model, and  $\lambda$  is the regularisation parameter.  $\|\mathbf{W}_m(\mathbf{m} - \mathbf{m}_0)\|_2^2$  can be interpreted as the roughness of the model, which quantifies the complexity or variation of the model.  $\|\mathbf{W}_d(\mathcal{F}(\mathbf{m}) - \mathbf{d})\|_2^2$  is the data misfit, which quantifies the difference between observed and modeled data and can include an error term. With the choice of  $\lambda$ , the trade-off between data misfit and model complexity can be controlled. Building on this foundation, several deterministic methods have been developed, such as Gauss-Newton inversion and Conjugate Gradient. A constraint inversion can be used to incorporate prior information about the model, which can be useful to prevent overfitting to noise. Stochastic methods, on the other hand, randomly search the solution space and provide a range of plausible models rather than a single deterministic solution. This is significantly more computationally expensive, but can be more robust against noise and can provide uncertainty estimates. Particle swarm optimization (PSO) and Bayesian inversion are examples of stochastic methods (Rücker et al. 2017; Xue et al. 2020).

An implementation of the deterministic approach is the PyGIMLi library, introduced by Rücker et al. (2017), which uses Gauss-Newton inversion to iteratively update the model parameters. PyGIMLi is an open-source library written in Python and C++ and is designed for the inversion of geophysical data. It allows the implementation of any given forward operator into the inversion algorithm, which makes it a versatile tool for geophysical modeling and inversion.

#### 2.1.5 L-curve method

Solving inverse problems is a task not limited to geophysics, which makes inversion theory an important field in mathematics. There are several methods to solve an inverse problem, but the most common approach is to use Tikhonov

regularisation (5). But the choice of the regularisation parameter  $\lambda$  is not trivial and can have a significant impact on the inversion result.

The L-curve method is widely used to determine the optimal  $\lambda$  for the solution of an inverse problem (Hansen 1999). The L-curve is a graph of the residual norm against the solution norm. With an increasing  $\lambda$ , the residual norm is expected to increase and the solution norm is expected to decrease. This leads to a curve that resembles an L-shape. An optimal  $\lambda$  should minimise the residual norm while keeping the solution norm small. This leads to the “corner” of the L, which is also the point with the highest curvature.

Lloyd et al. (1997) implements a method to find the point of maximum curvature and through this the optimal  $\lambda$  for the inversion of diffusion battery data. The method computes the  $\chi^2$ , also called “error weighted root-mean-square”, and the roughness of the model for different  $\lambda$  values to obtain the L-curve. A cubic spline function is fitted to the data points, to make it possible to calculate the curvature for each data point:

$$\mathbf{C}(\lambda_i) = \frac{d^2 s / dx^2}{(1 + (ds/dx)^2)^{3/2}} \quad (6)$$

$$x = \log_{10} \chi^2(\lambda_i)$$

and find the point with the maximum curvature. The corresponding  $\lambda$  is then considered the optimal one. This method was not developed for geophysical data, but a modell roughness and  $\chi^2$  can be computed for the TEM data as well.

A similar approach was used by Farquharson et al. (2004) to find the optimal  $\lambda$ . In this method the value of the regularization parameter  $\lambda$  is refined in each iteration of the data inversion. The inversion is started with a large  $\lambda$  and the L-curve is calculated. Then the curvature for the chosen  $\lambda$  is calculated through the formula:

$$\mathbf{C}(\lambda) = \frac{\zeta' \eta'' - \zeta'' \eta'}{[(\zeta')^2 + (\eta')^2]^{3/2}} \quad (7)$$

$$\zeta = \log \phi_d^{\text{lin}}$$

$$\eta = \log \phi_m$$

$\phi_d^{\text{lin}}$  is the data misfit and  $\phi_m$  is the model roughness. For the next iteration a new  $\lambda$  is calculated based on:

$$\lambda^n = \max(c\lambda^{n-1}, \lambda^{\max}) \quad (8)$$

where  $\lambda^n$  is the new  $\lambda$  value,  $\lambda^{n-1}$  is the previous  $\lambda$  value,  $0.01 \leq c \leq 0.5$  and  $\lambda^{\max}$  is the value for  $\lambda$ , which maximises the curvature. This cooling-schedule-type behaviour is added to prevent the inversion to skip to low values of  $\lambda$ , which is supposed to prevent artifacts created by overfitting the data. This method was tested on synthetic frequency domain electromagnetic data and was able to achieve an appropriate fit of inverted to the observed data.

Another approach for finding the optimal  $\lambda$  is the iterative golden section search as proposed by Cultrera et al. (2020). After providing an initial range for the optimal  $\lambda$   $[\lambda_1, \lambda_4]$ , two more  $\lambda$  values are calculated using the formula:

$$\varphi = \frac{1 + \sqrt{5}}{2}$$

$$\lambda_2 = 10^{\frac{\log_{10} \lambda_4 + \varphi \cdot \log_{10} \lambda_1}{1 + \varphi}} \quad (9)$$

$$\lambda_3 = 10^{\log_{10} \lambda_1 + (\log_{10} \lambda_4 - \log_{10} \lambda_2)}$$

For each  $\lambda$  the corresponding point on the L-curve is found and two curvatures ( $C_2$  and  $C_3$ ) are computed relying on three points each.  $C_2$  is the curvature of the points  $\lambda_1, \lambda_2$ , and  $\lambda_3$ .  $C_3$  is the curvature of the points  $\lambda_2, \lambda_3$ , and  $\lambda_4$ . Then  $\lambda_1$  or  $\lambda_4$  is omitted depending on which curvature is larger and a fourth  $\lambda$  is calculated based on the formula for  $\lambda_2$  (9). This process is repeated until the difference between the lambda-values of the interval are below a certain threshold. This method allows to find an optimal  $\lambda$  while minimising the number of inversions necessary. The search algorithm was tested with the ERT method on a conductive thin film with two non-conductive anomalies and showed promising results in finding the “corner” of the L-curve.

## 2.2 Experimental Set up

In order to investigate the applicability of automatically determining an optimal lambda value to TEM data, we conducted a field survey in October of 2024 at the Martenhofer Lacke in the

Nationalpark Neusiedlersee - Seewinkel. The Geophysics Research Unit at TU Wien kindly provided data from May 2024 for the same location but with a differing measuring configuration, which enables a comparison between varying setups.

Furthermore a python package was developed to read, filter, and invert the TEM data. The visualisation of an L-curve as well as several methods of automatically finding an optimal lambda were also implemented.

### 2.2.1 Measuring Device

Both survey were conducted with the TEM-Fast 48 HPC system by Applied Electromagnetic Research (AEMR). It is compact device allowing the use of a single-loop configuration. By connecting an external 12 / 24 V battery a current either 1 / 4 A can be put through the connected transmitter loop. It records up to 48 logarithmically spaced time gates, which results in a time range between 4–16000  $\mu$ s. The specific number of time gates can be chosen through a time-key. Table 2 shows which time-key leads to which recording time range. To provide an optimal signal-to-noise ratio the device automatically stacks multiple pulses (Barsukov et al. 2015). The number of stacks are given by the formula  $P_{tot} = 13 \times n_s \times n_{as}$  (Aigner et al. 2021), where  $n_s$  (1–20) is the chosen stacking-key and  $n_{as}$  is the number of analogue stacks depending on the chosen time-key and can be found in Table 2. More detailed information on the device can be found in the manual provided on the website <http://www.aemr.net/tem-fast.htm>.

### 2.2.2 Field Survey

The field measurements were carried out at the Martenhofer Lacke in the *Nationalpark Neusiedlersee - Seewinkel* ( $16^{\circ} 51' 23.05''$  N,  $47^{\circ} 45' 8.4348''$  E), which is located on the east side of the Neusiedler See, Austria. Being part of the Seewinkel, which are intermittent alkaline soda waters, this water cycle of this lake is fueled by deep saline groundwater and evaporation leading to its high salinity and shallow water depth, which also varies throughout the year (Boros et al. 2025). This location was chosen due to having sparse man-made structures in the Na-

tionalpark, which reduces noise in the gathered data to a minimum (Aigner et al. 2024).

The first survey, consisting of 45 soundings as shown in Figure 2 with a  $12.5 \times 12.5$  m loop, was carried out on the 22nd May 2024 and for the second survey 66 soundings, visualised in Figure 3 with a  $6.25 \times 6.25$  m loop were measured on 8th October 2024. For both surveys a Voltage of 24V was used and Table 3 shows the parameters for each sounding. Based upon a first visual inspection of the data some soundings were marked as "anomalous" as seen in Figures 2 and 3.

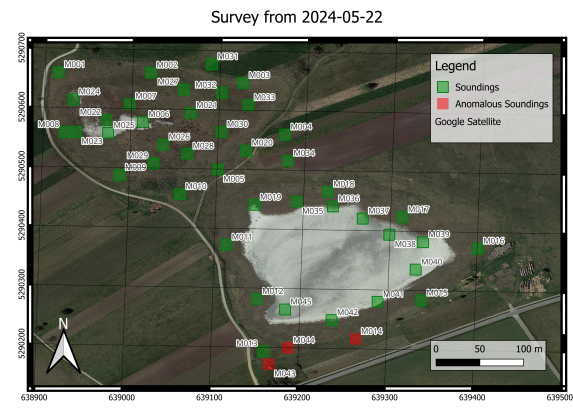


**Fig. 2:** Locations of all the TEM soundings measured in the first survey (22nd May 2024), where soundings are marked as anomalies, which fell out of order in a first visual inspection.

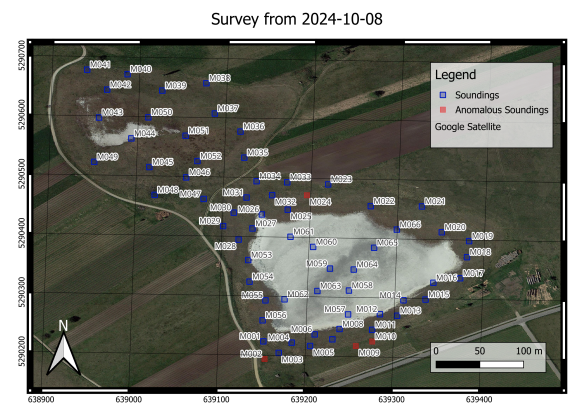


**Fig. 3:** Locations of all the TEM soundings measured in the second survey (8th October 2024), where soundings are marked as anomalies, which fell out of order in a first visual inspection.

**Tab. 2:** Parameters relating to the time-key of the TEM-FAST 48 HPC system (Excerpt from the manual).

Key	Max Time ( $\mu s$ )	Time Gates	Analogue Stacks
1	64	16	1024
2	128	20	512
3	256	24	256
4	512	28	128
5	1024	32	64
6	2048	36	32
7	4096	40	16
8	8192	44	8
9	16384	48	4

### 2.2.3 Python Package

In order to process the gathered data, we developed a python package mainly based on open-source python libraries. For the inversion routine we built upon the work of Aigner et al. (2021), which combines the electromagnetic wave modelling capabilities of `empymod` (Werthmüller 2017) with the inversion algorithm from `PyGIMLi` (Rücker et al. 2017).

The capabilities of this package include the reading of TEM data, adding coordinates to each sounding, the filtering based upon a time intervall, and the visualisation of the raw with the filtered data. The inversion routine requires certain starting parameters like the lambda value, a layer distribution, a start model, and the relative error of the measured signal. If not specified otherwise a homogeneous model with the median apparent resistivity of the sounding is used as the starting model and the relative error is computed based of the error output of the measuring device. In case of particularly noisy data it is possible to set a minimum value for the relative error (noise floor). The noise floor limits how strongly the inversion algorithm tries to fit the model to each data point to avoid fitting errors. This inversion algorithm works with a model of the subsurface, where a resistivity value is assigned to a layer with a certain thickness, and only modifies the resistivity value of every layer while keeping the thicknesses fixed. This makes the choice of an appropriate layer distribution (specifying the number and thicknesses of layers) vital (Welkens 2025).

We also implemented the functionality to compute and visualise an L-Curve for a TEM

sounding. For this we run the inversion for various logarithmically spaced lambda values, specified by the lower bound, the upper bound, and the number of values. For each inversion, we compute the root-mean-square (RMS) misfit of the data with the model as well as the roughness of the model and use these two values as the coordinates of a point corresponding to each inversion, which should result in an L-Curve (Cultrera et al. 2020; Hansen 1999).

To find an optimal lambda value for the inversion we implemented several search algorithms, which all try to find the point (corresponding to a lambda value) with the highest curvature on the L-Curve (Lloyd et al. 1997; Cultrera et al. 2020). We implemented the method used by Lloyd et al. (1997), which fits a cubic spline function to the L-Curve and computes the first and second derivative of this function, which are used to compute the curvature of the function at each point. We also implemented a similar approach, where we used the `numpy.gradient` function (<https://numpy.org/doc/1.26/reference/generated/numpy.gradient.html>) to compute the first and second derivative for the curvature. Lastly we implemented the iterative golden section search algorithm as described by Cultrera et al. (2020), where a lower and upper bound is defined for the lambda value and by comparing two curvatures within the interval and discarding the lower one, this method contracts the interval towards the optimal lambda. The advantage compared to the other two methods is that it is not bound to the predefined list of logarithmically spaced

**Tab. 3:** Device settings used as well as the resulting measured time ranges and total number of pulses stacked for each sounding of both surveys.

Sounding	Current	Time Range	Time Key	Stacking Key	Total Stacks
<b>22nd May 2024</b>					
M001, M002	4.1 A	4 – 480 $\mu$ s	4	3	4992
M003 – M014	1.0 A	4 – 480 $\mu$ s	4	3	4992
M015 – M045	1.0 A	4 – 240 $\mu$ s	3	3	9984
<b>8th October 2024</b>					
M001 – M066	4.1 A	4 – 240 $\mu$ s	3	5	16640

lambda values, which in theory allows a more precise determination of the optimal lambda.

## 3 Results

The data gathered in the two surveys was processed separately. Upon a visual inspection of apparent resistivity curves, which make minor differences more distinguishable than the signal curves, the soundings were split into two groups: The majority of soundings which follow a clear trend, which we will reference as "normal soundings" and some soundings which do not align with the trend will be referenced as "anomalous soundings".

### 3.1 Filtering of the Data

Figure 4 shows the normal soundings of the first survey (22nd May 2024) with the  $12.5 \times 12.5$  m loop and Figure 5 shows the anomalies. In Figure 4(b) it can be clearly seen that the effects of the turn-off ramp as described by Aigner et al. (2021) influence the measurements until about  $8 \mu$ s, which alignes with the  $4.2 – 8.6 \mu$ s, found by Aigner et al. (2021). At about  $240 \mu$ s Figure 4(b) shows how the various curves start having distortions and Figure 4(a) shows that measured impulse response is becoming a similar order of magnitude as the measured errors. For this reason the measurements are filtered to the time range of  $8 – 210 \mu$ s as shown in Figure 4(c) and (d). Figure 4(d) shows the pattern, that most curves first decline, but all curves increase in later times.

The apparent resistivities of the anomalous soundings as seen in Figure 5(b) show no clear pattern due to high distortions in the curves. These soundings (M014, M043, M044) are located close to a road as Figure 2 shows, which could explain the poor data quality. These anomalous measurements were still processed, to test how well they compare to the other

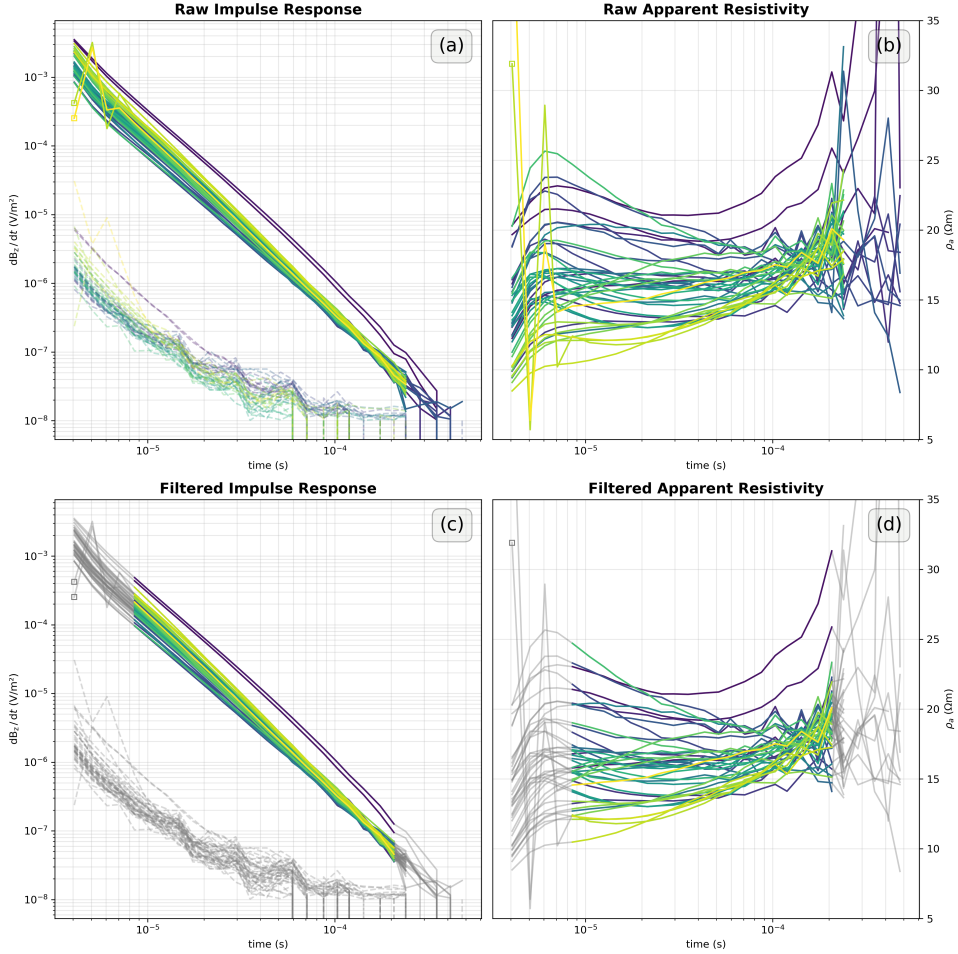


**Fig. 4:** Raw and filtered impulse responses and apparent resistivities from the 22nd May 2024 survey, where anomalies are excluded. The first sounding (M001) is colored dark purple, the last sounding (M045) is yellow, and all soundings in between are assigned a color from a uniform distribution between the two border colors. Subfigure (a) shows the raw impulse response as well as the measured errors as dashed lines, (b) shows the computed apparent resistivities, (c) show the filtered impulse response, the measured error as dashed lines, and greyed out raw data as comparison, (d) shows the resulting filtered apparent resistivities and greyed out raw values.

soundings. In order to make it more comparable the same time range of  $8 - 210 \mu\text{s}$  was used for the filtering (Figure 5(d)).

The normal soundings (Figure 6) and anomalies (Figure 7) of the second survey (8th October 2024) with the  $6.25 \times 6.25 \text{ m}$  loop were processed in a similar fashion. Compared to Figure 4(b) Figure 6(b) shows the effects of the turn-off ramp until  $12 \mu\text{s}$ , but only for the soundings within the lake (M057-M065, except for M062), while the other soundings show effects until  $7 \mu\text{s}$ , which should be a bit smaller for smaller loop sizes (Aigner et al. 2021). The long lasting effect of the turn-off ramp for the soundings

in the water, can on one side be attributed to a longer turn-off ramp in water (Aigner et al. 2021) and can on the other hand also be due to the loop being partially submerged during the measurements, which breaks the assumption of a layered halfspace, which is necessary for the computation for the apparent resistivity as well as the data inversion (Kirsch 2006). Due to the smaller loop size, the curves become distorted much earlier at about  $85 \mu\text{s}$  (Figure 6(b)) and at that time the impulse response also becomes the same order of magnitude as the measured error (Figure 6(a)). In order to make processing easier the soundings in and next to the lake

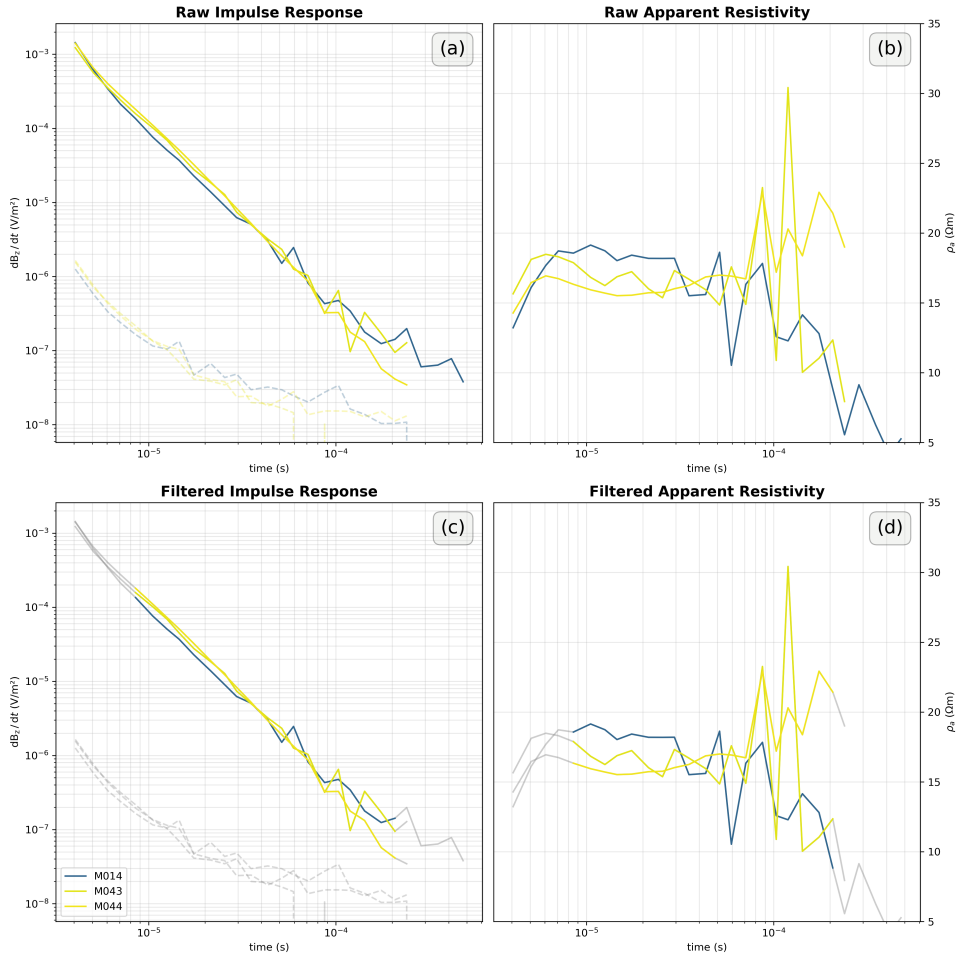


**Fig. 5:** The anomalous raw and filtered impulse responses and apparent resistivities from the 22nd May 2024 survey. Subfigure (a) shows the raw impuls response as well as the measured errors as dashed lines, (b) shows the computed apparent resistivities, (c) show the filtered impulse response, the measured error as dashed lines, and greyed out raw data as comparison, (d) shows the resulting filtered apparent resistivities and greyed out raw values.

were both filtered to the time range  $12 - 80 \mu\text{s}$  as shown in Figure 6(c) and (d). Figure 6(d) shows that in contrast to the soundings with the larger loop, the curves only show the incline at the end, but not the decline in the beginning.

For the second survey the anomalous soundings, shown in Figure 7, include the soundings M009 and M010, which show distortions, but also M002, which has much lower apparent resistivities (about  $10 - 15 \Omega\text{m}$  less) compared to the other soundings, and M024, which has much higher apparent resistivities (about  $15 - 30 \Omega\text{m}$  higher) compared to the other soundings. For the anomalous soundings the same time range of  $12 - 80 \mu\text{s}$  was used for the filtering (Figure 6(c) and (d)). Figure 7(d) shows that due

to the distortions no clear pattern can be seen in the soundings M009 and M010, M024 shows a much steeper incline than the other soundings (Figure 6(d)), and M002 shows a decline in the apparent resistivity curve. Figure 3 shows that M009 and M010 are close to a road and M002 is close to a vineyard containing metall bars.

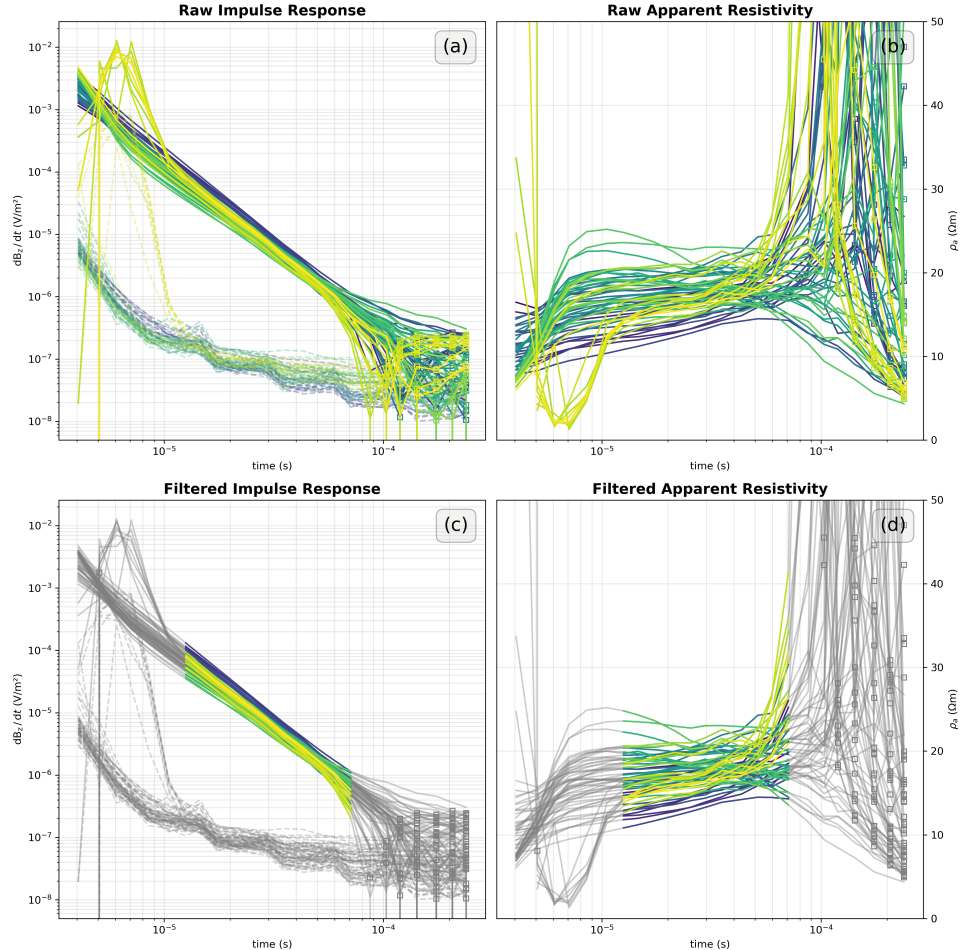


**Fig. 6:** Raw and filtered impulse responses and apparent resistivities from the 8th October 2024 survey, where anomalies are excluded. The first sounding (M001) is colored dark purple, the last sounding (M066) is yellow, and all soundings in between are assigned a color from a uniform distribution between the two border colors. Subfigure (a) shows the raw impulse response as well as the measured errors as dashed lines, (b) shows the computed apparent resistivities, (c) shows the filtered impulse response, the measured error as dashed lines, and greyed out raw data as comparison, (d) shows the resulting filtered apparent resistivities and greyed out raw values.

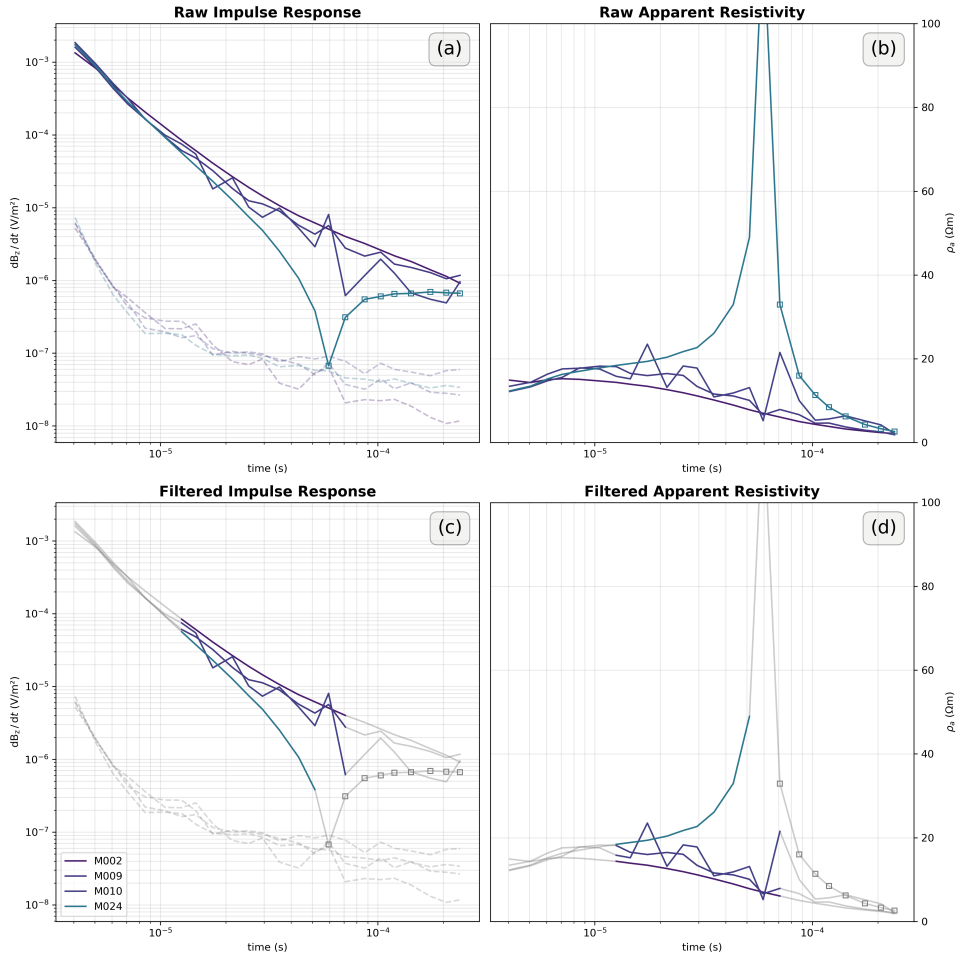


**Fig. 7:** The anomalous raw and filtered impulse responses and apparent resistivities from the 8th October 2024 survey. Subfigure (a) shows the raw impuls response as well as the measured errors as dashed lines, (b) shows the computed apparent resistivities, (c) show the filtered impulse response, the measured error as dashed lines, and greyed out raw data as comparison, (d) shows the resulting filtered apparent resistivities and greyed out raw values.

### 3.2 Inversion Parameters

The inversion algorithm (Aigner et al. 2021) used for the inversion needs various starting parameters. One of which is the layer distribution, which specifies the number and thicknesses of the layers characterising the subsurface model, which is used for the inversion. Welkens (2025) shows that model with 1 m-Layers until 5 m depth and 1.5 m-Layers below that, until a maximal depth of 10 m optimises the inversion speed and model fit for data gathered with a  $6.25 \times 6.25$  m loop and 4.1 A of current. Since a  $12.5 \times 12.5$  m loop is used in the first survey and

Figure 8(c) shows that the inversion algorithm struggles to fit the late time data. Figure 9(c) shows that this issue can be resolved by choosing a maximal depth of 10 m.

Regarding the noise floor, the minimum value for the relative error used in the inversion, Aigner et al. (2024) used 1.5 – 2.5 % for the measurements with a  $12.5 \times 12.5$  m and a  $50.0 \times 50.0$  m loop the in the soda lakes and 3 – 15 % for the soundings at the ice glacier. For the first survey with the  $12.5 \times 12.5$  m loop a noise floor of 2.5 % was chosen because this measurement configuration resembles the configuration with the smaller loop by Aigner et al. (2024). For the second survey with the  $6.25 \times 6.25$  m loop the noise floor was set to 8.0 % because smaller loop sizes decreases the magnetic moment, which leads to a smaller signal-to-noise ratio and thus to less reliable measurements (Kirsch 2006).

To compute the L-Curve and find an optimal lambda value for the inversion, a range of logarithmically spaced lambda values was chosen with the lower boundary of 10, the upper boundary of 1000, and a total of 20 values. This range covers the lambda values Aigner et al. (2024) used for the inversion of the data gathered in the soda lakes (50) and the former graphite mine (500 to 1000). By choosing 20 values in total total computation time is kept low, while the characteristics of each L-Curve can still be resolved (Figure 10).

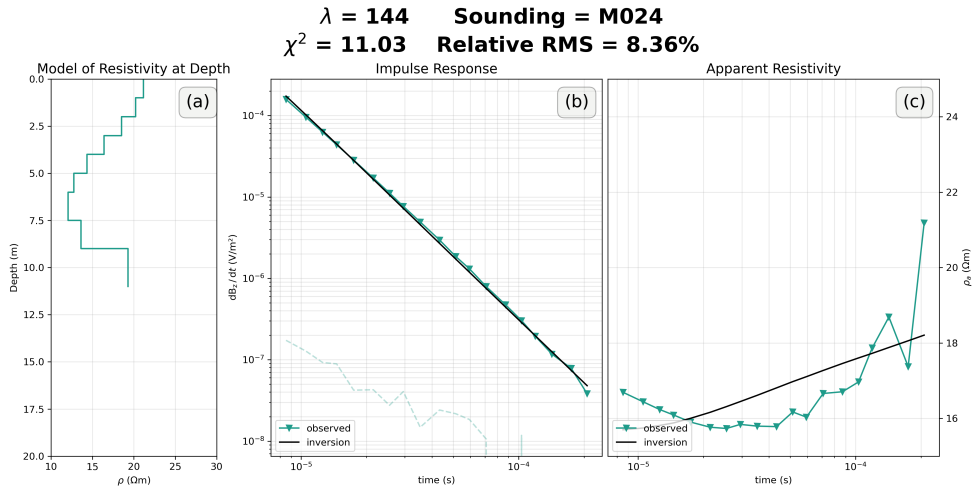


**Fig. 8:** Inversion results for a representative sounding (M024) for the first survey (22nd May 2024) with the layer distribution of 1 m thicknesses until 5 m depth and 1.5 m until 10 m depth. Subfigure (a) shows the final subsurface model of the resistivity, (b) shows the comparison between the modelled and measured impulse response as well as the measured error as a dashed line, (c) shows the comparison between the modelled and measured apparent resistivities.

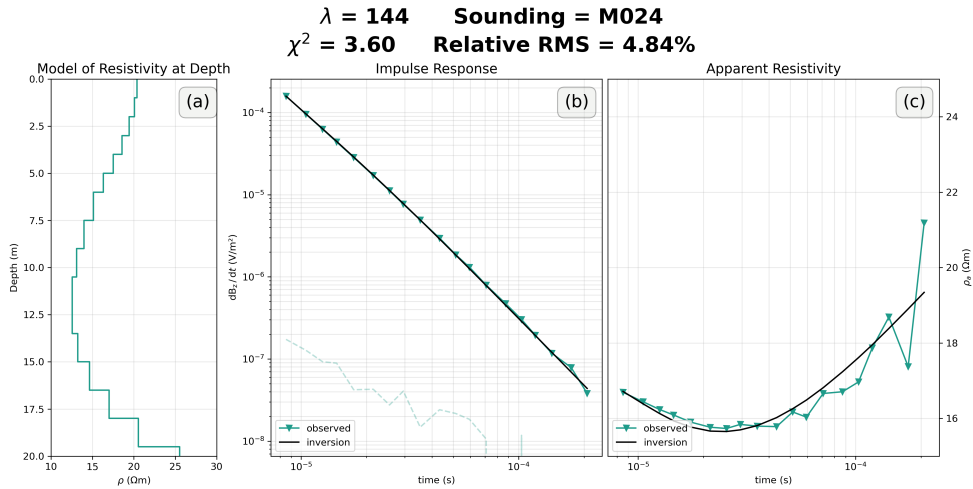


**Fig. 9:** Inversion results for a representative sounding (M024) for the first survey (22nd May 2024) with the layer distribution of 1 m thicknesses until 5 m depth and 1.5 m until 20 m depth. Subfigure (a) shows the final subsurface model of the resistivity, (b) shows the comparison between the modelled and measured impulse response as well as the measured error as a dashed line, (c) shows the comparison between the modelled and measured apparent resistivities.

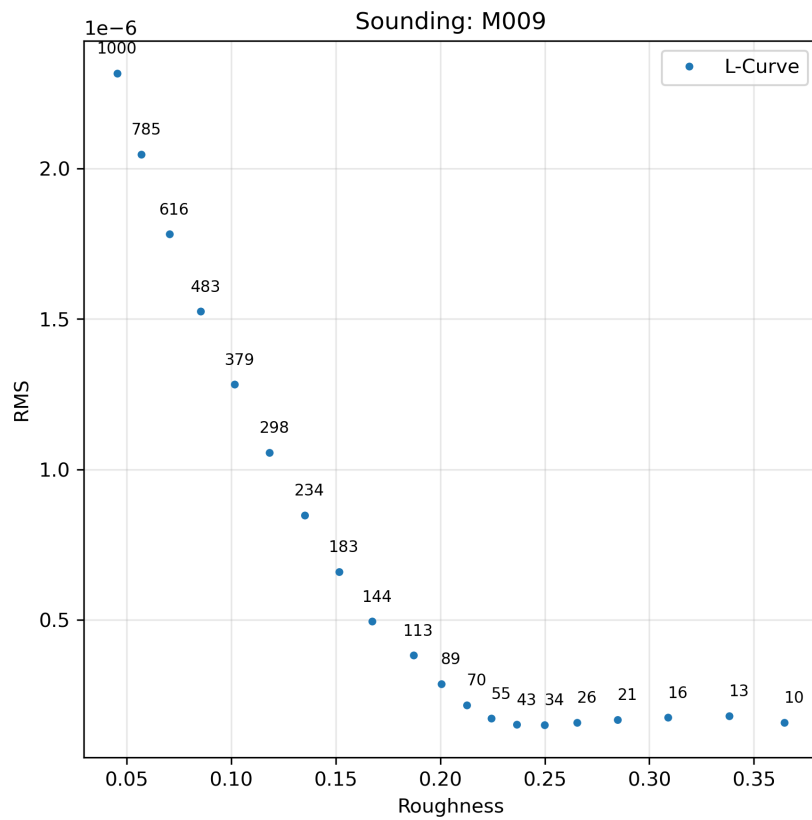


**Fig. 10:** L-Curve of the sounding M009 of the first survey (22nd May 2024) showcasing the chosen distribution of lambda values. The number next to each point is the corresponding lambda value. The y-axis shows the root-mean-square (RMS) misfit between the model and the measured data. The x-axis shows the roughness of the model.

### 3.3 Finding an Optimal Lambda

Figure 10 shows that the RMS misfit ( $0.1 - 2.5e-6$ ) and the roughness ( $0.04 - 0.37$ ) are of entirely different orders of magnitude. To highlight this issue the various search algorithms were applied to the sounding M010 of the first survey, shown in Figure 12, where due to its minor curvature all three algorithms return a too high lambda value between  $483 - 616$  as opposed to the visual optimum at about 33.6. To counteract this a linear normalisation, using the formula  $a_i = \frac{a_i - a_{\min}}{a_{\max} - a_{\min}}$ , was applied to both RMS and roughness. Figure 12 shows how with the normalisation all three search algorithms return a value ( $25 - 43$ ) around the visual optimum of 33.6. Hence all further searches for an optimal lambda were carried out with the normalisation.

Figure 10 shows how the ideal L-Curve would look like as it was described by Hansen (1999) and Farquharson et al. (2004), but TEM data gathered in the field always includes some level of noise, which can lead differently shaped resulting curves from this computation. One extreme example can be seen in Figure 13, which resembles a random cluster of points rather than an L-Curve, which makes discerning an optimal lambda not feasible. Both the cubic spline as well as the gradient based algorithm find a local

minimum (Figure 13), but as the plotted data points do not create a cohesive L-Curve, hence the returned values not be considered the actual optimal lambda for the inversion.

Another example where the L-curve differs from the ideal can be seen in Figure 14, which shows an minimum at the lambda value 379 and an increase in the RMS misfit afterwards until the lambda value 55. This could possibly be explained by the inversion algorithm trying to fit the model to an error in the measured data, which would explain the increase in the RMS misfit. Figure 14 shows that both the cubic spline and gradient based algorithm can find this minimum. Only the golden section search fails, which can be explained by the minimum being close to the upper boundry and thus being discarded in the first iteration of the search algorithm. Cultrera et al. (2020) described that the first two lambda values within the interval are calculated using the golden section method, which in this case excludes the lambda value associated with the minimum.

Another eventuality can be seen in Figure 15, where the curve shows a discontinuity between the lambda values 43 and 34, where the RMS misfit abruptly decreases by about 70 %. Figure 15 shows that the golden section search and the gradient based algorithm can still find this optimal lambda value, but the cubic spline algorithm can not and returns a value before the discontinuity.

An additional case is shown by Figure 16, where the roughness values start to decrease again after the lambda value of about 20 and thus "looping back". This could be caused by the inversion algorithm trying to fit the erroneous data points and thus prioritising outliers over following the general trend. If for example an outlier opposes a general trend, which indicates a multiple layers with differing resistivities, then by fitting the outlier leads to a more homogeneous model and thus a decrease in the model roughness. Figure 16 shows that the golden section search returns the lambda value at the turning point as opposed to the actual optimum, which both the cubic spline and gradient based algorithms return.

These examples highlight the strengths and shortcomings of each search algorithm. Table 4 shows a summary of how the algorithms

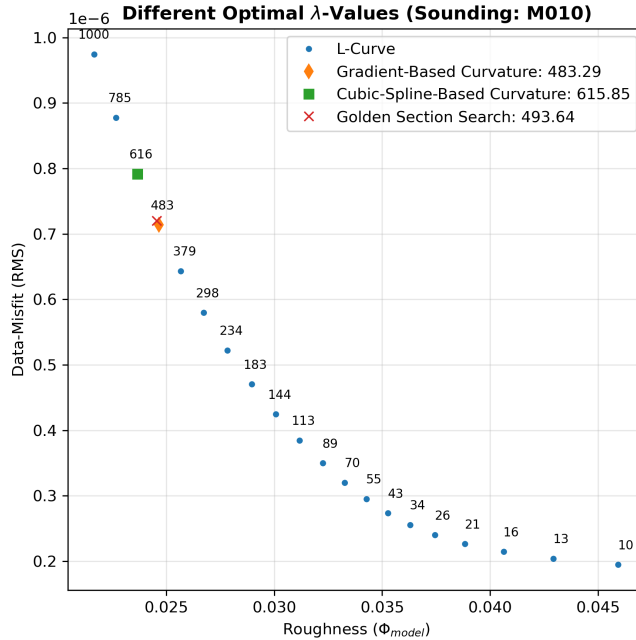


**Fig. 11:** Automatically searching for an optimal lambda of the sounding M010 in the first survey (22nd May 2024) without applying a normalisation to the L-Curve.

performed overall and comparing this to a visual inspection of the generated L-Curve. In both surveys 7 out of 111 soundings produce a curve, which can not be used to find an optimal lambda, even when visually inspected. The golden section search found the least optimal lambdas, only 57 out of 111, but when it worked, it returned the most accurate results by finding the optimal lambda accurately down to first decimal point. The cubic spline algorithm was more reliable overall by finding 83 out of 111 optimal lambdas, but as Figure 15 shows it also struggles with suboptimal L-Curves. In our analysis the gradient based curvature analysis yielded the most promising results by finding 89 out of 111 optimal lambda values, hence it was used to find the optimal lambda for each sounding respectively. As all search algorithms maximise the curvature of the L-Curve to find the lambda, all of them struggle with curves with minimal curvature or even linear graphs. Table 4 also shows that there are minimal differences in the produced L-Curves as well as the effectiveness of the automated search algorithms between the two surveys and thus the two measuring configurations. All comparison plots can be found at [https://github.com/pb-tuwien/BSc\\_Soda\\_Lakes\\_Balogh.git](https://github.com/pb-tuwien/BSc_Soda_Lakes_Balogh.git)

under "data/2024xxxx/TEMdata/07-inversion\_analysis/comparison\_M0yy.png", where xxxx is either "0522" for the first or "1008" for the second survey and yy being the sounding number (either 01 to 45 or 01 to 66).

**Tab. 4:** Summary of the search for an optimal lambda for each sounding, comparing the visual identification with the various automated search algorithms.

Search Type	Found	Not Found
<b>22nd May 2024</b>		
Visual	42	3
Cubic Spline	32	13
Gradient Based	34	11
Golden Section	19	26
<b>8th October 2024</b>		
Visual	62	4
Cubic Spline	51	15
Gradient Based	55	11
Golden Section	38	28

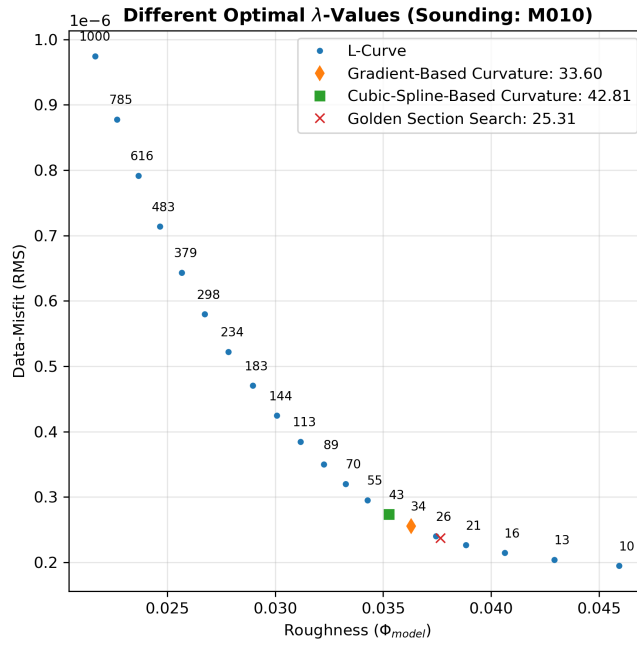


**Fig. 12:** Automatically searching for an optimal lambda of the sounding M010 in the first survey (22nd May 2024) while applying a normalisation to the L-Curve.

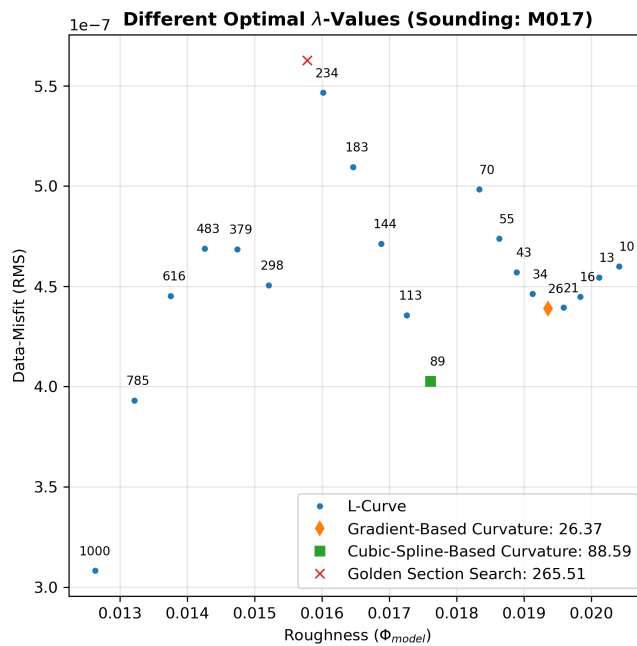


**Fig. 13:** Automatically searching for an optimal lambda of the sounding M017 in the first survey (22nd May 2024), which showcases how the search algorithms perform, when no expected characteristic of an L-curve can be found.

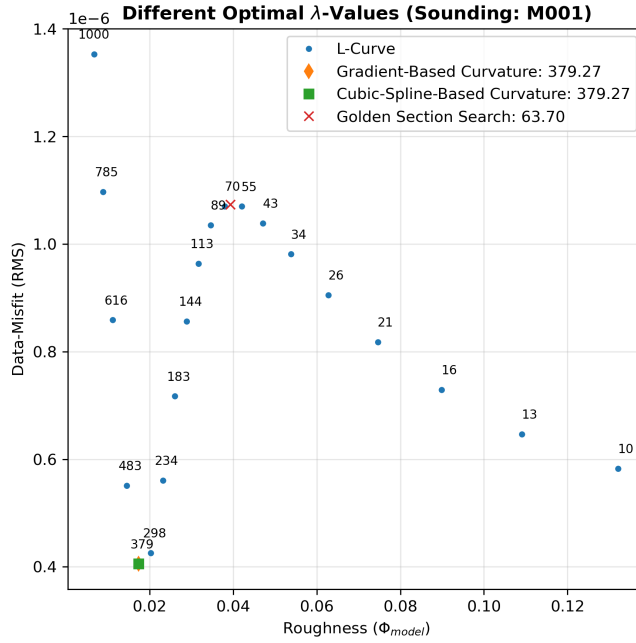


**Fig. 14:** Automatically searching for an optimal lambda of the sounding M001 in the second survey (8th October 2024), which showcases that the golden section search algorithm is unable to identify a minimum close to a boundary.

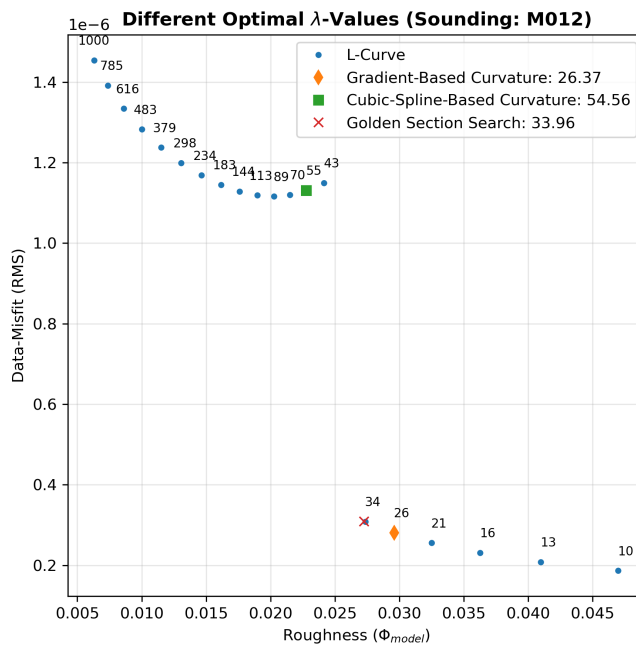


**Fig. 15:** Automatically searching for an optimal lambda of the sounding M012 in the second survey (8th October 2024), which showcases that the search algorithm fitting a cubic spline function can not optimise the lambda for an L-Curve with a discontinuity.

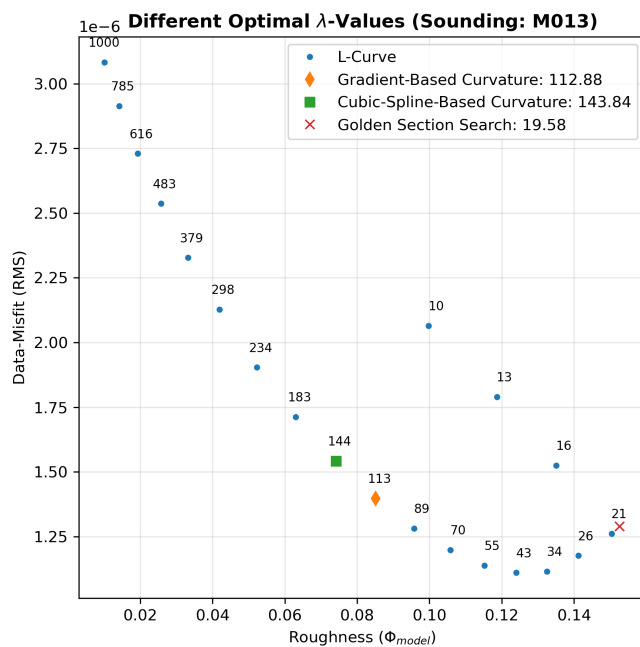


**Fig. 16:** Automatically searching for an optimal lambda of the sounding M013 in the first survey (22nd May 2024), which showcases how the golden section search algorithm fails, when L-curve shows an inverted C-shape on the end.

### 3.4 Comparing Inversion Results

With these findings, we finally obtained the necessary parameters for running the inversions, which enables a comparison of different resistivity models obtained from the various measuring configurations, as described in Table 3. Because the late time data was filtered due to a high noise level, the different time keys are not considered and only the different injected currents and the loop sizes are compared. Ideally the compared soundings, would be at the same location, which is why we chose the soundings M028 (shown in Figure 17) of the first and M052 (shown in Figure 18) of the second survey, which use the  $12.5 \times 12.5$  m loop with 1.0 A of current and  $6.25 \times 6.25$  m loop with 4.1 A of current. Figures 2 and 3 show that these two broadly align. For the configuration  $12.5 \times 12.5$  m loop with 4.1 A of current we do not have a sounding at the same location, but sounding M002 (shown in Figure 19) of the first survey is also in the north of the Martenhofer Lacke (Figure 2). Figure 17(c) shows how with the large loop three distinct layers can be found: A 5 m-layer with  $17.5 \Omega\text{m}$ , a second 11 m-layer with  $13.5 \Omega\text{m}$ , and the start of a third layer with  $22 \Omega\text{m}$ . The model seems to fit the data adequately as can

be seen in Figure 17(a) and (b), which is also supported by a relative RMS misfit of 4.77 %.

For the same location five months later the small loop with 4.1 A produces a model with only two discernable layers, as seen in Figure 18(c): A 5 m-layer with  $16 \Omega\text{m}$  and the start of a second layer with  $24 \Omega\text{m}$ . The second layer is not distinctly visible, but rather a gradual increase, which corresponds with the almost linearly increasing apparent resistivity curve in Figure 18(b). Figure 18(a) and (b) also show that the last measured data point possibly indicates a change in the slope and thus a new layer (Fitterman et al. 1986), but it could also be data noise.

Figure 19 represents the measurements made with the large loop as well as 4.1 A and in (c) similar three layers can be seen as in Figure 17(c) but with differing resistivity values: A 5 m-layer with  $31 \Omega\text{m}$ , a second 12 m-layer with  $13.5 \Omega\text{m}$ , and the start of a third layer with  $30 \Omega\text{m}$ . Figure 19(b) shows that the model does not quite fit the measured data, but follows the general trend of the curve.

We found that the measurements with the  $12.5 \times 12.5$  m loop were able to discern the same three layers regarding the thicknesses, which Aigner et al. (2024) found in a borehole at the soda lakes, which is located about 1.5 km north-east of the Martenhofer Lacke. Aigner et al. (2024) describes a 1.6 m clay-silt layer, followed by a 5.4 m sandy gravel aquifer, and a second clay-silt layer until the maximal drilled depth of 10 m. Figures 17 and 19 both show in subfigure (c) that the first two layers of the borehole can not be differentiated and are shown as one layer with the resistivities of  $31 \Omega\text{m}$  and  $17.5 \Omega\text{m}$  respectively. These differences could be caused by differing clay-silt layer and aquifer thicknesses, which also changes the influence of each over the resistivity value representing the combined resistivities of both layers. The second layer present in the subfigures (c) of Figures 17 and 19 shows a layer with a resistivity of about  $13.5 \Omega\text{m}$ , which points to a clay-silt layer when compared with the values in Table 1

(Referencing table with common resistivity from the State of the Art). This agrees well with the borehole data described by Aigner et al. (2024). The third layer with the resistivity

of  $22\Omega\text{m}$  and  $30\Omega\text{m}$  respectively, could indicate a second aquifer, which was also detected by Aigner et al. (2024), who found that a second aquifer with the resistivity value of  $30\Omega\text{m}$  at a depth below 35 m.

The model created through the data gathered with the  $6.25 \times 6.25\text{ m}$  loop, as seen in Figure 18, only shows the first two layers and is unable to resolve the third layer. The advantage of being able to resolve shallow layers with a smaller loop (Kirsch 2006), is counteracted by the effects of turn-off ramp as described by Aigner et al. (2021) and thus the need to discard the early time data. The results produced with the larger loop and the current of  $4.1\text{ A}$  seem to reproduce the results of earlier studies like Aigner et al. (2024) the best out of the configurations tested in this work.

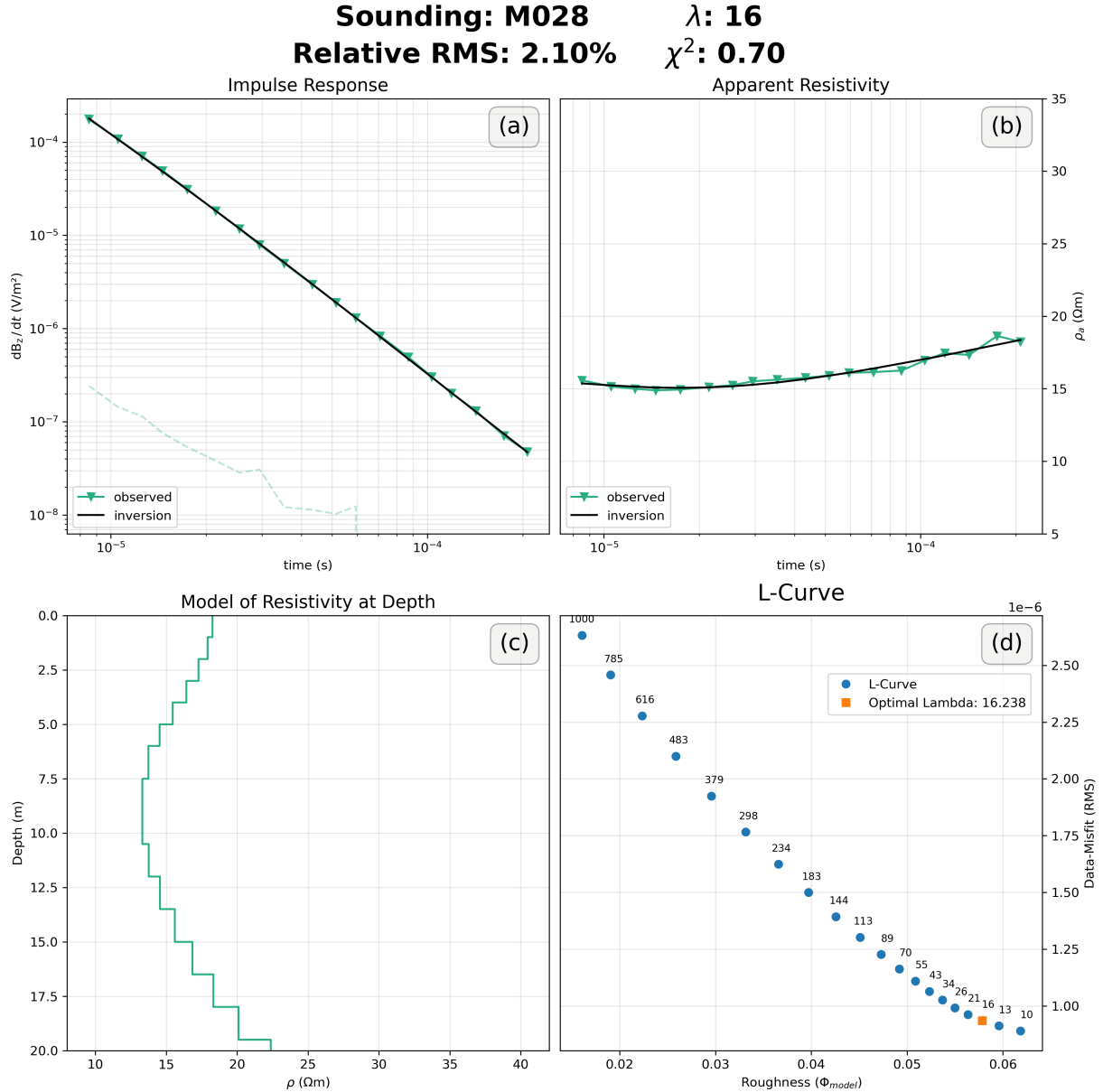


**Fig. 17:** Optimised inversion of the sounding M028 of the first survey, which was measured with a  $12.5 \times 12.5$  m loop and 1.0 A of current. This sounding was done at the same location as M052 of the second survey. Subfigure (a) shows the comparison between modelled and measured impulse response as well as the measured error, (b) shows the comparison between modelled and measured apparent resistivities, (c) shows the final subsurface model of the resistivity, (d) shows the L-curve of this sounding with the chosen lambda value marked in orange.

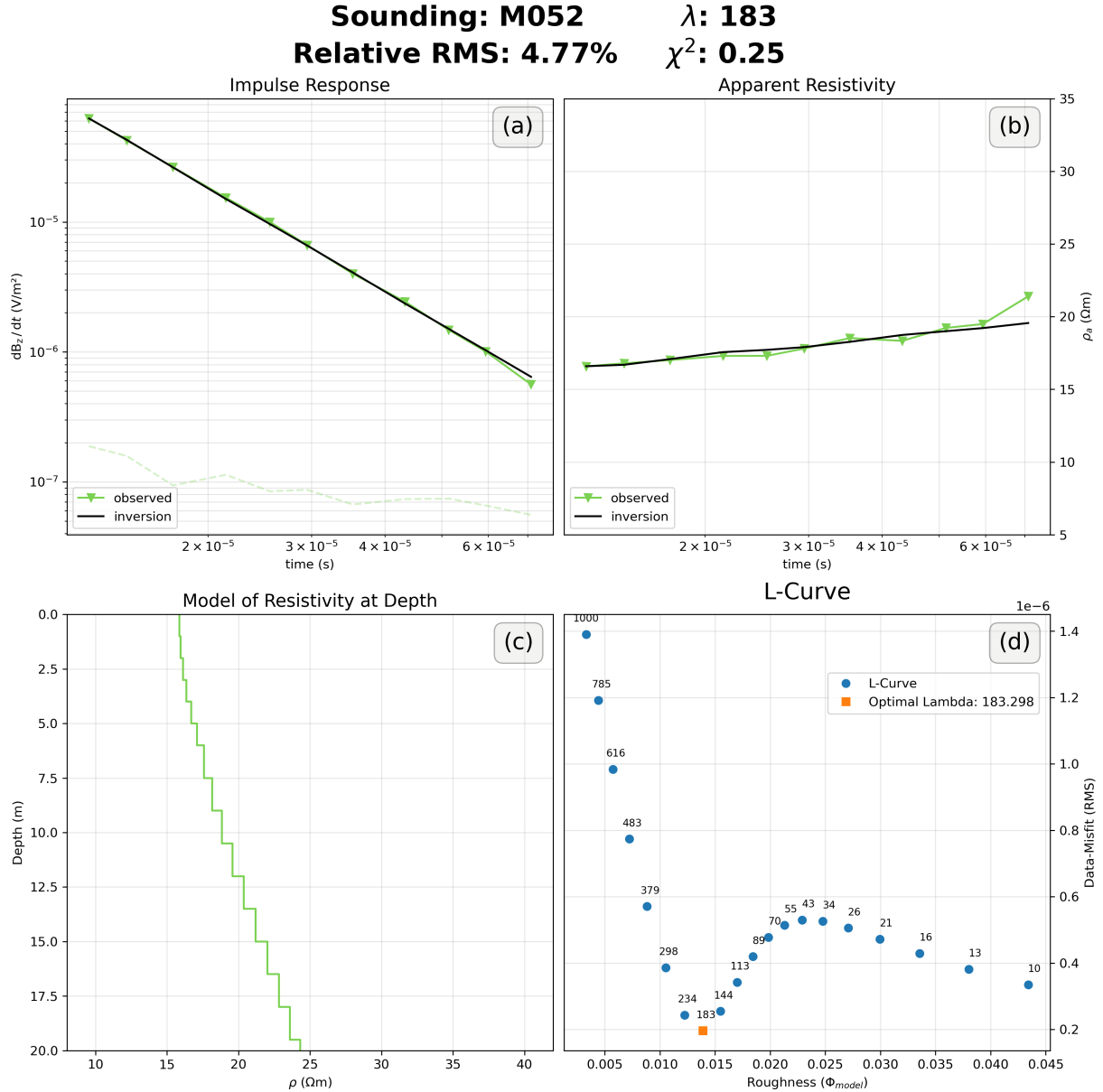


**Fig. 18:** Optimised inversion of the sounding M052 of the second survey, which was measured with a  $6.25 \times 6.25$  m loop and 4.1 A of current. This sounding was done at the same location as M028 of the first survey. Subfigure (a) shows the comparison between modelled and measured impulse response as well as the measured error, (b) shows the comparison between modelled and measured apparent resistivities, (c) shows the final subsurface model of the resistivity, (d) shows the L-curve of this sounding with the chosen lambda value marked in orange.

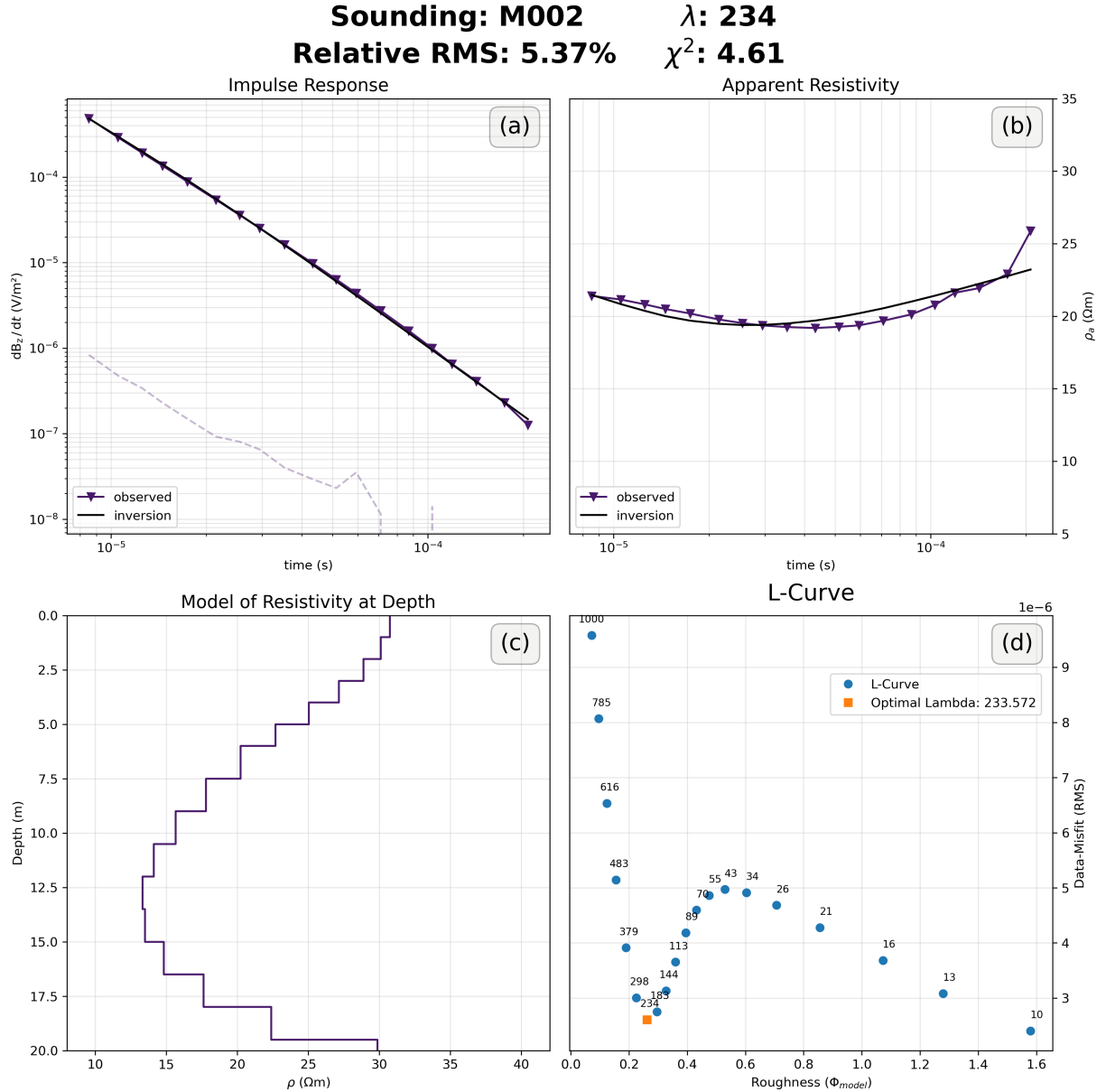


**Fig. 19:** Optimised inversion of the sounding M002 of the first survey, which was measured with a  $12.5 \times 12.5$  m loop and 4.1 A of current. Subfigure (a) shows the comparison between modelled and measured impulse response as well as the measured error, (b) shows the comparison between modelled and measured apparent resistivities, (c) shows the final subsurface model of the resistivity, (d) shows the L-curve of this sounding with the chosen lambda value marked in orange.

## 4 Conclusion

### List of Figures

1	Numerically modelled typical TEM response with the signal a) and the apparent resistivity b).	3
2	Map of Sounding Locations in May	7
3	Map of Sounding Locations in October . . . . .	7
4	Response Curves of the May Survey	10
5	Anomalous Responses of the May Survey . . . . .	11
6	Response Curves of the October Survey . . . . .	12
7	Anomalous Responses of the October Survey . . . . .	13
8	Inversion With 10m Maximum Depth . . . . .	15
9	Inversion With 20m Maximum Depth . . . . .	15
10	Example L-Curve . . . . .	16
11	Lambda Search Without Normalisation . . . . .	18
12	Lambda Search With Normalisation . . . . .	19
13	Example Lambda Search: Bad Curve . . . . .	19
14	Example Lambda Search: Minimum Close to Boundry . . . . .	20
15	Example Lambda Search: Curve With a Discontinuity . . . . .	20
16	Example Lambda Search: Curve With a "Loop-Back" . . . . .	21
17	Inversion of Sounding with the Large Loop and Small Current . . . . .	24
18	Inversion of Sounding with the Small Loop and Large Current . . . . .	25
19	Inversion of Sounding with the Large Loop and Large Current . . . . .	26

### List of Tables

1	Common Resistivity Values of Subsurface Materials . . . . .	1
2	Time Key Parameters of the TEM-FAST Device . . . . .	8
3	Device Settings in Both Surveys	9
4	Summary of the search for an optimal Lambda . . . . .	18

### Declaration of competing interest

The authors declare that they have no known competing financial interests or personal relationships that could have appeared to influence the work reported in this thesis.

### Data availability

The python package for this thesis was developed in cooperation with Jakob Welkens and is building upon the routine from Aigner et al. (2021). It is available open-source and can be accessed on github ([https://github.com/pb-tuwien/Bsc\\_TEM\\_tools.git](https://github.com/pb-tuwien/Bsc_TEM_tools.git)). To facilitate full reproducibility of the results all data and python routines used throughout this work can also be accessed on github ([https://github.com/pb-tuwien/BSc\\_Soda\\_Lakes\\_Balogh.git](https://github.com/pb-tuwien/BSc_Soda_Lakes_Balogh.git))

### References

- Aigner, L., P. Högenauer, M. Bücker, and A. Flores Orozco (2021). “A flexible single loop setup for water-borne transient electromagnetic sounding applications”. In: *Sensors* 21.19, p. 6624.
- Aigner, L., D. Werthmüller, and A. F. Orozco (2024). “Sensitivity analysis of inverted model parameters from transient electromagnetic measurements affected by induced polarization effects”. In: *Journal of Applied Geophysics* 223, p. 105334.
- Auken, E., N. Foged, J. J. Larsen, K. V. T. Lassen, P. K. Maurya, S. M. Dath, and T. T. Eiskjær (2019). “tTEM—A towed transient electromagnetic system for detailed 3D imaging of the top 70 m of the subsurface”. In: *Geophysics* 84.1, E13–E22.
- Barsukov, P. O., E. B. Fainberg, and E. O. Khabensky (2015). “Shallow investigations by TEM-FAST technique: methodology and examples”. In: *Electromagnetic sounding of the Earth's interior*. Elsevier, pp. 47–78.
- Boros, E. and L. Vörös (2025). “How can unique alkaline soda waters be managed and restored? Lake Neusiedl as the largest threatened european example”. In: *Ecohydrology* 18.2, e2738.

- Christiansen, A. V., E. Auken, and K. Sørensen (2006). "The transient electromagnetic method". In: *Groundwater geophysics: a tool for hydrogeology*. Springer, pp. 179–225.
- Cutrera, A. and L. Callegaro (2020). "A simple algorithm to find the L-curve corner in the regularisation of ill-posed inverse problems". In: *IOP SciNotes* 1.2, p. 025004.
- Danielsen, J. E., E. Auken, F. Jørgensen, V. Søndergaard, and K. I. Sørensen (2003). "The application of the transient electromagnetic method in hydrogeophysical surveys". In: *Journal of applied geophysics* 53.4, pp. 181–198.
- Farquharson, C. G. and D. W. Oldenburg (2004). "A comparison of automatic techniques for estimating the regularization parameter in non-linear inverse problems". In: *Geophysical Journal International* 156.3, pp. 411–425.
- Fitterman, D. V. and M. T. Stewart (1986). "Transient electromagnetic sounding for groundwater". In: *Geophysics* 51.4, pp. 995–1005.
- Galazoulas, E. C., Y. C. Mertzanides, C. P. Petalas, and E. K. Kargiotis (2015). "Large scale electrical resistivity tomography survey correlated to hydrogeological data for mapping groundwater salinization: a case study from a multilayered coastal aquifer in Rhodope, Northeastern Greece". In: *Environmental processes* 2, pp. 19–35.
- George, N., A. Ekanem, J. Thomas, and T. Harry (2021). "Modelling the effect of geo-matrix conduction on the bulk and pore water resistivity in hydrogeological sedimentary beddings". In: *Modeling Earth Systems and Environment*, pp. 1–15.
- Gómez, E., M. Larsson, T. Dahlin, G. Barmen, and J.-E. Rosberg (2019). "Alluvial aquifer thickness and bedrock structure delineation by electromagnetic methods in the highlands of Bolivia". In: *Environmental Earth Sciences* 78, pp. 1–13.
- Gonzales Amaya, A., J. Mårdh, and T. Dahlin (2018). "Delimiting a saline water zone in Quaternary fluvial-alluvial deposits using transient electromagnetic: a case study in Punata, Bolivia". In: *Environmental earth sciences* 77, pp. 1–9.
- Hansen, P. C. (1999). "The L-curve and its use in the numerical treatment of inverse problems". In.
- Kirsch, R. (2006). *Groundwater geophysics: a tool for hydrogeology*. Springer.
- Lloyd, J., C. Taylor, R. Lawson, and R. Shields (1997). "The use of the L-curve method in the inversion of diffusion battery data". In: *Journal of aerosol science* 28.7, pp. 1251–1264.
- Rücker, C., T. Günther, and F. M. Wagner (2017). "pyGIMLi: An open-source library for modelling and inversion in geophysics". In: *Computers & Geosciences* 109, pp. 106–123.
- Sørensen, K. I. and E. Auken (2004). "SkyTEM—A new high-resolution helicopter transient electromagnetic system". In: *Exploration Geophysics* 35.3, pp. 191–199.
- Su, M., M. Chu, Y. Xue, X. Ma, and Z. Ju (2024). "Response analysis and application of the TEM using small-fixed loops". In: *Acta Geotechnica* 19.6, pp. 3537–3553.
- Welkens, J. (2025). "Comparison of subsurface geophysical models of Hutweidenlacke (Nationalpark Seewinkel) based on the Transient Electromagnetic Method". MA thesis. Research Unit Geophysics, Department of Geodesy and Geoinformation, TU Wien, Vienna, Austria.
- Werthmüller, D. (2017). "An open-source full 3D electromagnetic modeler for 1D VTI media in Python: empymod". In: *Geophysics* 82.6, WB9–WB19. DOI: 10.1190/geo2016-0626.1. URL: <https://doi.org/10.1190/geo2016-0626.1>.
- Xue, G., H. Li, Y. He, J. Xue, and X. Wu (2020). "Development of the inversion method for transient electromagnetic data". In: *IEEE Access* 8, pp. 146172–146181.
- Zhdanov, M. S. (2002). *Geophysical inverse theory and regularization problems*. Vol. 36. Elsevier.
- Zhou, Y., P. Jianwei, L. Hao, W. Zhongmei, Z. Jiang, L. Haixin, and L. Jiaxu (2022). "Multi-turn small-loop transient electromagnetic data processing using constraints from borehole and electrical resistivity tomography data". In: *Arabian Journal of Geosciences* 15.22, p. 1675.